THE JOURNAL OF PHYSICAL CHEMISTRY LETTERS
A JOURNAL OF THE AMERICAN CHEMICAL SOCIETY

pubs.acs.org/JPCL

Letter

Improving Near-Infrared Emission of *meso*-Aryldipyrrin Indium(III) Complexes via Annulation Bridging: Excited-State Dynamics

Aaron Forde, Levi Lystrom, Wenfang Sun, Dmitri Kilin, and Svetlana Kilina*

Cite This: *J. Phys. Chem. Lett.* 2022, 13, 9210−9220

Read Online

ACCESS | Metrics & More | Article Recommendations | Supporting Information

ABSTRACT: Using non-adiabatic dynamics and Redfield theory, we predicted the optical spectra, radiative and nonradiative decay rates, and photoluminescence quantum yields (PLQYs) for In(III) dipyrrin-based complexes (i) with electron-withdrawing (EW) or electron-donating (ED) substituents on the *meso*-phenyl group and (ii) upon fusing the pyrrin and phenyl rings via saturated or unsaturated bridging to increase structural rigidity. The ED groups lead to a primary π,π^* character with a minor intraligand charge transfer (ILCT) contribution to the emissive state, while EW groups increase the ILCT contribution and red-shift the luminescence to ∼1.5 eV. Saturated annulation enhances the PLQYs for complexes with primary π,π^* character compared to those of the non-annulated and unsaturated−annulated complexes, while both unsaturated and saturated annulation decrease the PLQYs for complexes with primary ILCT character. We found that PLQY improvement goes beyond a simple concept of structural rigidity. In contrast, the charge transfer character of excitonic states is a key parameter for engineering the NIR emission of In(III) dipyrrin complexes.

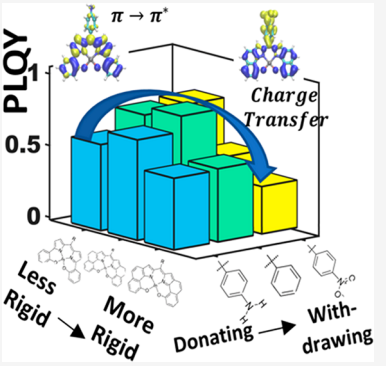

Near-infrared (NIR) absorbing and emissive materials are important for applications in night-vision-readable displays, light-emitting diodes (LED), telecommunication, optical sensing, photocatalysis, bioimaging, and photodynamic therapy (PDT).[1,2] Metallodipyrromethenes (M-DIPYs)[3] and metalloazadipyrromethenes (M-aza-DIPYs)[3] are classes of metal−organic complexes that have received a significant amount of attention in recent years due to their promising emission properties, which can be extended to the NIR regions[4,5] by various structural modifications on pyrrole rings in the DIPY ligands.[6,7]

There is an inherent difficulty in designing materials with efficient NIR luminescence. With a decrease in the transition energy, a significantly increased contribution from the nonradiative recombination of charge carriers is expected. This phenomenon is generally termed the "energy gap law".[8,9] An intuitive solution is to increase the structural rigidity, which can suppress the nonradiative decay pathways and enhance the NIR emission.[10] From this point of view, the tetracoordinating N_2O_2-type *meso*-aryldipyrrin (N_2O_2-*m*ADIPY) ligands are particularly interesting because they increase the structural rigidity of the formed complexes, resulting in deep-red emissive complexes when coordinated with group 13 and 14 elements.[4,11] In particular, an In(III) complex containing a *meso*-mesityl-N_2O_2-DIPY ligand exhibits a high photoluminescence quantum yield (PLQY) of ≤67% at 639 nm in a toluene/methanol [95:5 (v/v)] solution.[11]

Our recent calculations based on linear response time-dependent density functional theory (TDDFT) have predicted that both replacing oxygen in N_2O_2-*m*ADIPY with nitrogen in N_4-*m*ADIPY and functionalization at the *meso* position by phenyl rings with strong electron-withdrawing (EW) substituents or extending π-conjugation of the *meso*-aryl group result in red-shifting of the fluorescence energy of the In(III) complexes to the NIR regions of 750−960 nm and the lowest absorption band to 560−630 nm.[12] This trend is rationalized by a stronger shift of the electron density on the *meso*-aryl group with an improvement in the EW ability of the substituent on it or by extending the π-conjugation, which reduces the energy of the optical transition. These computational findings are encouraging results, providing important insights into the effect of substituents at the *meso*-aryldipyrrin on the optical response of the In(III) complexes. However, information about the radiative and nonradiative pathways controlling the PLQY in realistic compounds is missing from these calculations.

The analytical gradient TDDFT (AG-TDDFT)[13,14] provides geometry optimization of the electronic excited state and has been shown to be sufficient for predicting reasonable trends of the emission energies for Ir(III),[15] Ru(II),[16,17] Pt(II),[18] and Fe(II)[19,20] complexes upon variation of the substituents on the ligands to rationalize the experimental findings. However,

Received: July 7, 2022
Accepted: September 9, 2022
Published: September 28, 2022

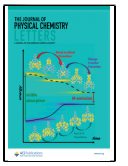

https://doi.org/10.1021/acs.jpclett.2c02115
J. Phys. Chem. Lett. 2022, 13, 9210−9220

accurate estimations of PLQY require the computation of radiative and nonradiative recombination rates between the lowest singlet excited-state (S_1) potential energy surface (PES) and the ground-state (S_0) PES. For this, one needs to go beyond the Born−Oppenheimer approximation (BOA), which neglects interactions between the electronic and vibrational degrees of freedom. Beyond BOA, one computes the non-adiabatic (NA) couplings along an excited-state trajectory, which determine the rates of nonradiative transitions. However, due to the high computational cost of NA couplings, the non-adiabatic molecular dynamics (NAMD) are limited for metal−organic complexes with extended π-conjugation and have been primarily applied for describing the pathways of energy transfer in metal-free dyadic[21] and dendritic[22,23] chromophores.

Here we apply the DFT-based NAMD using Redfield theory[24,25] to compute PLQY in a series of In(III)-based N_2O_2-*m*ADIPYs, which has been shown to be effective for modeling luminescent semiconducting nanomaterials.[26,27] In particular, we investigated the impact of dipyrrin ligand functionalization on the nonradiative and radiative dynamics of charge carriers with the specific aim of increasing PLQY through structural modifications of the ligand. We hope to decrease the level of nonradiative recombination by increasing structural rigidity while shifting the emission energy toward the NIR region.

Our previous TDDFT calculations[12] have shown that substitution of oxygen in N_2O_2-*m*ADIPY with nitrogen in N_4-*m*ADIPY with strong EW substituents at the *meso*-phenyl group on DIPY resulted in the most red-shifted fluorescence (725−961 nm) in In(III) complexes. However, the oscillator strength of the optical transition contributing to the fluorescence of In(III) N_4-*m*ADIPY is weak, compared to that of the corresponding In(III) N_2O_2-*m*ADIPY counterpart. Because the oscillator strength of the lowest optical transition is proportional to the radiative rates,[28] N_4-*m*ADIPY ligands are not the best candidates for NIR emission with high PLQYs. This behavior is rationalized by a larger change in the nearly tetrahedral geometry at the ground state to a more planar geometry at the excited state of the In(III) complexes with N_4-*m*ADIPY ligands, compared to the corresponding complexes with N_2O_2-*m*ADIPY ligands that have less pronounced changes between the ground and excited states with distorted square-planar geometry. Therefore, we consider only the In(III) N_2O_2-*m*ADIPY complexes in this work, which provides better conditions for radiative rates.

To understand the effect of the structural rigidity on both radiative and nonradiative processes in these complexes, we vary the rigidity of the molecules by annulation bridging of the pyrrole and phenyl groups in the N_2O_2-*m*ADIPY ligands. As shown in Scheme 1, the In(III) complexes labeled by **a** represent the structures with N_2O_2-*m*ADIPY without bridging (the least rigid structures), by **b** refer to N_2O_2-*m*ADIPY where the phenyl and pyrrole are annulated with a saturated bridging (more rigid structures), and by **c** indicate N_2O_2-*m*ADIPY that has unsaturated bridging (the most rigid structures). We also vary the substituent at position 4 of the *meso*-phenyl group on N_2O_2-*m*ADIPY from electron-donating (ED) groups in complexes **1** and **2** to electron-withdrawing (EW) groups in complexes **4** and **5**. In total, this gives 15 complexes to be simulated in this study.

To understand how changes in ligand structures impact the photophysical properties of the In(III) complexes, we

Scheme 1. In(III) N_2O_2-*m*ADIPY Complexes with Varying Annulations Connecting the Pyrrole and Phenyl Rings (a−c) and *meso*-Aryl Substituents (1−5) with Different ED and EW Abilities[a]

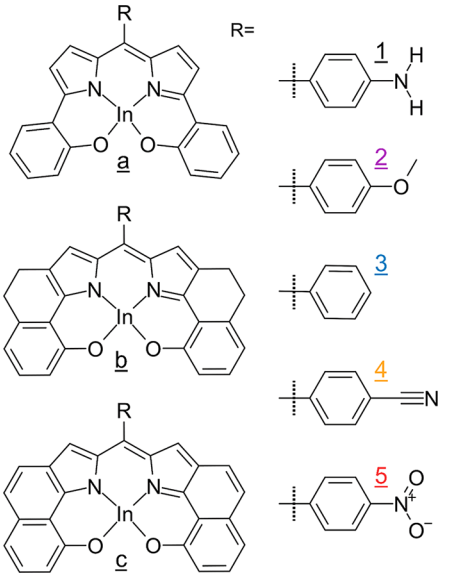

[a]The dashed lines indicate the connecting point of the aryl substituents corresponding to R.

performed TDDFT calculations of the absorbing and emissive electronic states using the PBE0 functional and mixed 6-31g*/LANL2DZ basis set in an acetonitrile solvent (see details in Methods). Figure 1 and Figure S1 show the computed absorption spectra along with the emission energies for all studied complexes. For each annulation approach, it is observed that there is a consistent red-shift of the onset of the absorption spectra (the trend is shown by a solid arrow in Figure 1) and the emission energy (the trend is shown by a dashed arrow in Figure 1) with the improved EW ability of the substituent. For both absorption and emission, the lowest-energy transition S_1 is drastically red-shifted for the most rigid complexes **c** (Figure S1).

Inspection of the natural transition orbitals (NTOs) contributing to lowest-energy optical transition S_1 shows that the stronger the EW ability of the substituent at the *meso*-phenyl group, the stronger the shift of electron density from the N_2O_2-*m*ADIPY region to the substituted *meso*-phenyl motif (Table 1 and Tables S1 and S2). This increases the intraligand charge transfer (ILCT) character of the S_1 state, resulting in a pronounced red-shift in the absorption and emission, which also agrees with our previous findings.[6] While all complexes demonstrate mixed π,π^* and ILCT characters of their S_1 states, the predominant contributor of these two types of optical transition varies when the nature of the substituent changes. In general, the ILCT character increases in the S_1 state with the improved EW ability of the substituent at the *meso*-phenyl group, which significantly lowers the S_1 energy. Increasing structural rigidity from series **a** complexes without annulation to series **b** and **c** complexes with saturated and unsaturated annulation, respectively, also causes a further red-shift of the lowest-energy absorption band and reduces the emission energies. This red-shift can be rationalized by the increased level of conjugation in the ligand because annulation induces a stronger delocalization of an electron−hole pair over the whole

https://doi.org/10.1021/acs.jpclett.2c02115
J. Phys. Chem. Lett. 2022, 13, 9210−9220

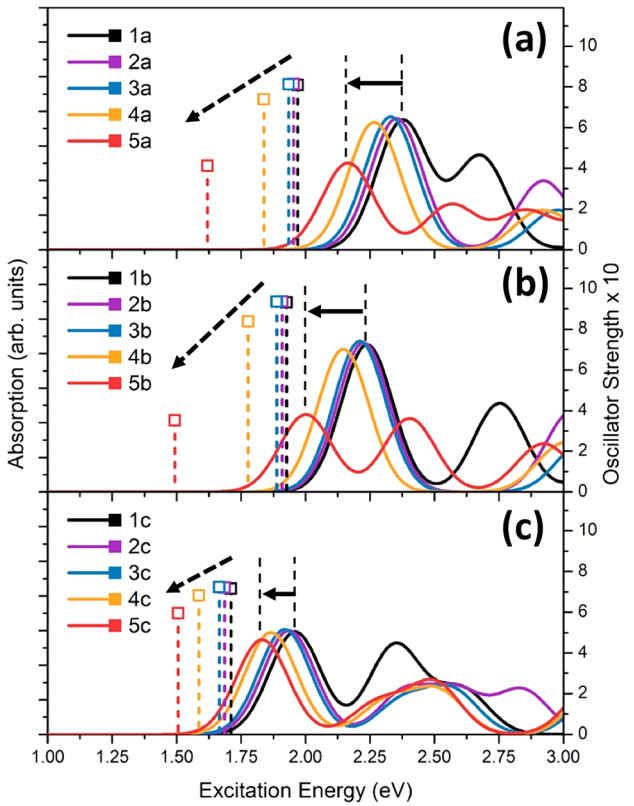

Figure 1. Absorption spectra (solid lines) and emission energies (dashed vertical lines) of all studied In(III) N_2O_2-*m*ADIPY complexes calculated using TDDFT and AG-TDDFT in acetonitrile, respectively: (a) complexes **1a**−**5a** without annulation, (b) complexes **1b**−**5b** with saturated annulation, and (c) complexes **1c**−**5c** with unsaturated annulation labeled consistently with Scheme 1, along with varying ED/EW strengths of the substituents at the *meso*-phenyl groups (**1**−**5**). The values of the oscillator strength for optical transitions are shown on the right *Y*-axis. For each series of annulations, there is a consistent red-shift of the absorption spectra (a solid black arrow) and the emission energy (a dashed black arrow) of the lowest-energy transition S_1 and its optical intensity with the improved EW ability of the substituent at the *meso*-phenyl group.

dipyrrin part of the ligand (Table 1). Overall, the extent of ILCT character accounts for the red-shift of the S1 transition and is closely associated with the strength of the EW group and the type of annulation, allowing tunability of the absorption and emission energies from 2.38 to 1.83 eV and from 1.97 to 1.51 eV, respectively.

This behavior can be rationalized by the ground-state electronic structure of the complexes, as shown in Figure 2. Improving the EW ability of the substituent at the *meso*-phenyl groups in **1**−**5** for the **b** series decreases the energy of LUMO, because the electron density distribution delocalizes over the *meso*-phenyl group with the improved EW ability of the substituent on it. However, the HOMOs in these complexes are negligibly affected by the substituent due to the localization of electron density mainly on the N_2O_2-*m*ADIPY part (Figure S2). This leads to a decrease in the HOMO−LUMO gap from 2.68 eV for **1b** to 2.42 eV for **5b** (Figure 2a). Considering the effect of annulation (as illustrated in Figure 2b), going from **3a** to **3c** by hybridizing with the frontier molecular orbitals of ethene results in delocalization of HOMO and LUMO along the bridged N_2O_2-*m*ADIPY parts accompanied by a noticeable decrease in the energy gap by 0.41 eV. In contrast, upon hybridization with ethane the resultant HOMO and LUMO for **3b** remain largely localized on the initial N_2O_2-*m*ADIPY ligand, resulting in an energy gap that is slightly reduced by 0.14 eV. This trend emerges for all complexes investigated, where EW substituents reduce the HOMO−LUMO energy gap due to a much stronger stabilization of the LUMO in comparison to that of the HOMO, while annulation with conjugated bridging slightly destabilizes the HOMO accompanied by a significant stabilization of the LUMO, leading to a further reduced HOMO−LUMO gap (Figures S2−S4).

Interestingly, the emission energy is more affected by the EW ability of the substituent at the *meso*-phenyl group (0.12−0.28 eV) compared to the impact on lowest transition state S_1 (0.30−0.36 eV) in absorption (Figure 1 and Figure S1) for series **a** and **b** complexes without and with saturated annulation with respect to the trend observed in series **c** complexes with unsaturated annulation. The difference in the trends between the lowest absorption and emission energies points out the difference in the geometry of complexes at the ground and excited states, which are more pronounced for series **a** complexes with EW substituents (**4** and **5**) as the least rigid structures. This trend is evidenced by the averaged values of the root-mean-square deviation between the ground- and excited-state geometries shown in Tables S3 and S4.

The difference between excited- and ground-state geometries points out the importance of Franck−Condon (FC) factors, the overlap between vibrational states of two electronic states. Figure 3 shows vibrationally resolved absorption and luminescence spectra calculated using TDDFT and AG-TDDFT, respectively, which include FC corrections for the S_1 transition in series **c** complexes, with those for series **a** and **b** are shown in Figure S5 and Table S5. The main trend that can be highlighted is that the enhanced EW ability of the substituent at the *meso*-phenyl group increases the relative intensity of the vibronic sideband, marked as $\mathbf{A_2}'$ and $\mathbf{F_2}'$ in Figure 3, compared to the pure electronic $\mathbf{A_1}$ and $\mathbf{F_1}$ bands. In addition, the Stokes shift also increases with the improved EW ability of the substituent. Both trends indicate that electron-vibrational couplings increase as the EW ability of the substituent at the *meso*-phenyl group improves and would be detrimental for NIR emission.

To estimate which of the complexes has the highest PLQY, we include both radiative and nonradiative processes in our calculations using NAMD to parametrize the Redfield theory, as explained in detail in Methods (the initial conditions of the NAMD trajectories are shown in Table S6). Figure 4 compares the room-temperature intraband relaxation dynamics of electrons (electron cooling) and related photoluminescence (PL) spectra for complexes **3a**−**c** with a dominating π,π^* character and **5a**−**c** with a significant ILCT character in their lowest-energy optical transitions. The character of these transitions is shown and discussed in Table 1 and Table S2. The increased ILCT nature of the lowest-energy transitions is manifested by the reduced intensity of the PL peaks, which are the most pronounced for annulated complexes **5b** and **5c** (Figure 4d), compared to those of complexes **3** (Figure 4c). Notably, for complexes **1** and **3** with large π,π^* character in the lowest optical transitions, saturated annulation increases the PL intensity. For complexes **5** with substantial ILCT character, the PL intensity decreases with both saturated and unsaturated annulations (Figure 4d and Figure S6).

For complex **3b**, the saturated annulation slows electron cooling (a green line in Figure 4a). However, unsaturated

https://doi.org/10.1021/acs.jpclett.2c02115
J. Phys. Chem. Lett. 2022, 13, 9210−9220

Table 1. Natural Transition Orbitals (NTOs) Representing the Excited Electron−Hole Pair Contributing to Lowest-Energy Optical Transition S_1 of the Absorption and Emission Spectra of Complexes 1, 3, and 5[a]

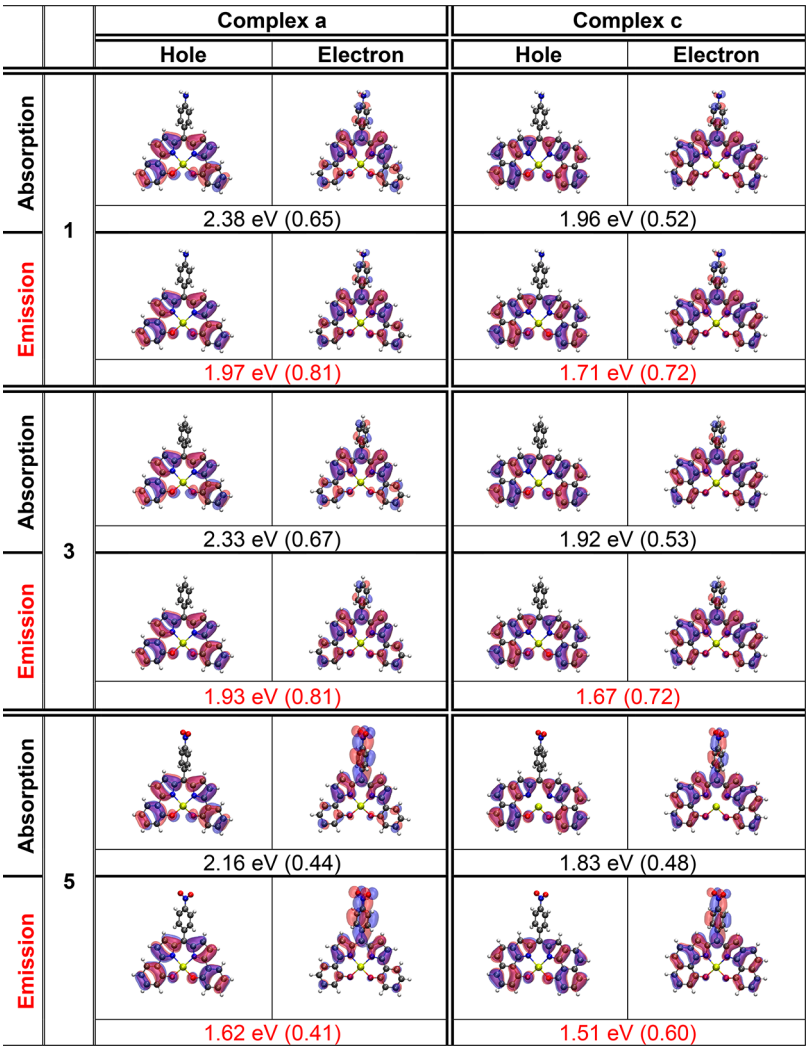

[a]Values in parentheses represent computed oscillator strengths.

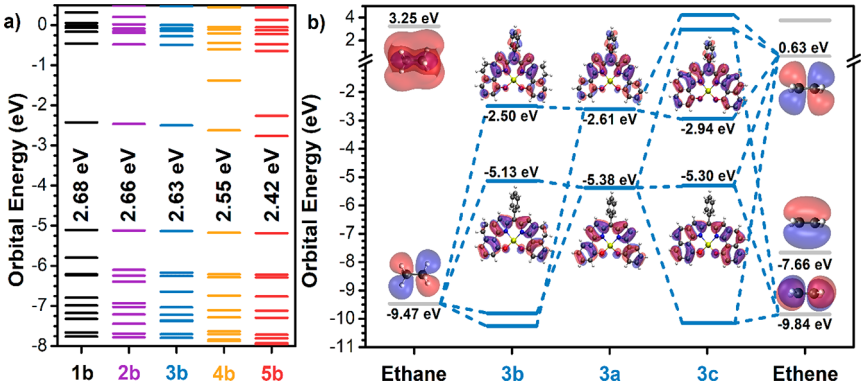

Figure 2. Ground-state electronic structure of selected complexes for demonstration of the decrease in the HOMO−LUMO energy gap with the improved EW ability of the substituent at the *meso*-phenyl group and with annulation. (a) The ground-state molecular orbital energy diagram for complexes **1b**−**5b** shows significant stabilization of LUMO energies with the improved EW ability of the substituents, resulting in a reduced energy gap. (b) Visualization of the frontier orbitals of complexes **3a**−**c** with various bridging annulation and ethane and ethene molecules. Annulation via ethene (**3c**) provides conjugation through the annulated portion of the N_2O_2-*m*ADIPY ligand, which increases the level of delocalization of the HOMO and LUMO orbitals and reduces the energy gap. Ethane provides saturated bonding (**3b**) across the annulated portion of the complex, which keeps the charge density in the N_2O_2-*m*ADIPY part only and insignificantly changes the energy gap.

https://doi.org/10.1021/acs.jpclett.2c02115
J. Phys. Chem. Lett. 2022, 13, 9210−9220

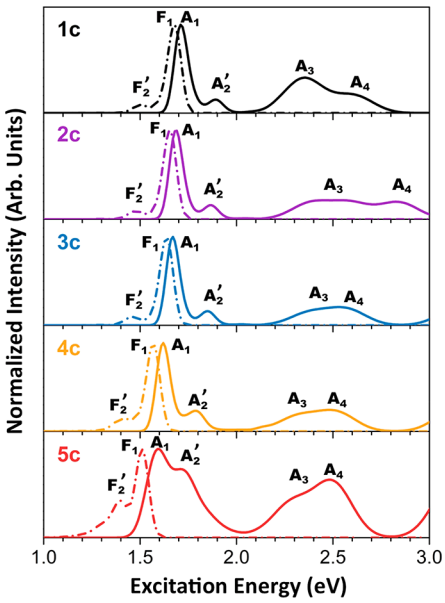

Figure 3. Vibrationally resolved absorption (solid lines) and fluorescence (dashed−dotted lines) spectra with Franck−Condon corrections being included for the S_1 electronic transition computed for complexes **1c**−**5c** upon variation of the substituents from ED (top) to EW (bottom) groups at the *meso*-phenyl motif on the N_2O_2-*m*ADIPY ligands. Peaks in the absorption (fluorescence) spectra corresponding to electronic transitions are labeled as A_n (F_n), while A_2' (F_2') corresponds to the vibronic sideband.

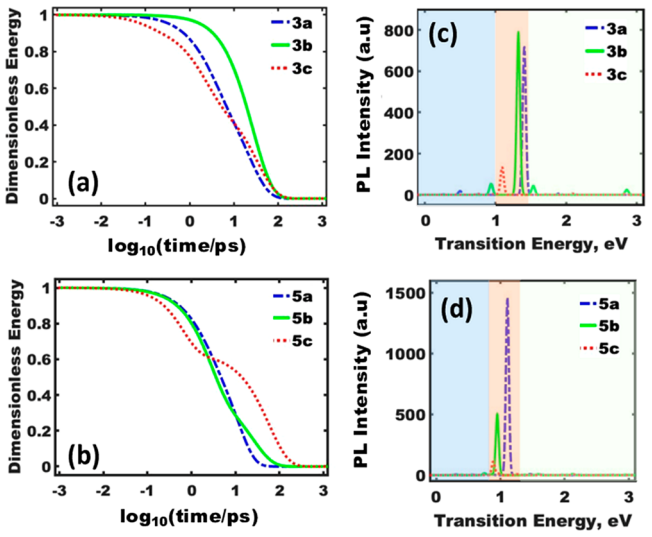

Figure 4. Transient and steady-state observables along the photo-induced excited-state trajectory. Hot-electron cooling and radiative relaxation along the excited-state trajectory for (a and c) complexes **3a**−**c** without substituents and (b and d) complexes **5a**−**c** with the strongest EW NO_2 substituent and without (blue dashed−dotted lines), with saturated (green solid lines), and with unsaturated (red dotted lines) annulation. In panels c and d, the light-orange-shaded regions represent the emission from S_1 states and the light-blue-shaded regions with low-intensity peaks correspond to transient luminescence along the excited-state trajectory.

annulation results in electron cooling comparable to that of the non-annulated complex (a red line for **3c** vs a blue line for **3a** in Figure 4a). In contrast, complexes **5a**−**c** with the strongest EW substituent exhibit a distinct change in the decay kinetics (Figure 4b). For non-annulated complex **5a** (a blue line in Figure 4b), the kinetics are single-exponential in character similar to those in complexes **3**, while for the annulated complexes, the decays become slow and biexponential, which is most saliently observed for **5c** with the unsaturated annulation (a red line in Figure 4b).

Figure 5 provides an explanation for this biexponential behavior. We compare the intraband relaxation dynamics of a

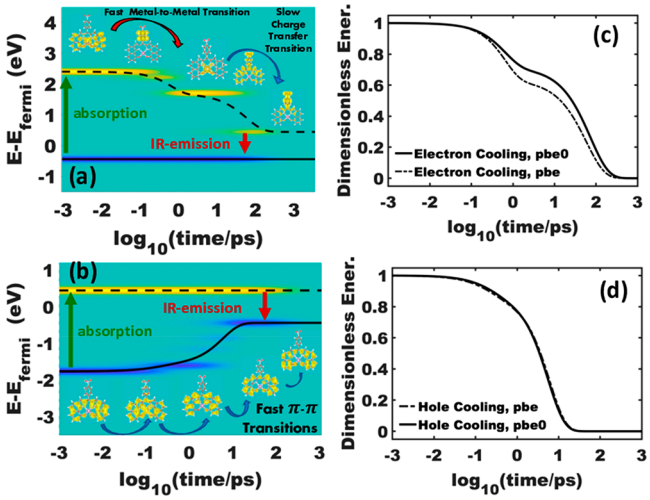

Figure 5. Nonradiative intraband dynamics of an excited electron−hole pair in complex **5c**. (a) Hot-electron cooling and (b) hot-hole cooling calculated by NAMD using the PBE functional. Time evolution of the initially excited electron (yellow) and hole (blue) charge density with the dark cyan representing ground states. The black line represents the ensemble average energy for the electron (a dashed line) and hole (a solid line) relaxation. Insets of panels a and b show Kohn−Sham orbitals corresponding to the mostly occupied electronic (hole) states during relaxation. We compare PBE-computed nonradiative relaxation to those calculated by hybrid functional PBE0 for (c) hot-electron and (d) hot-hole cooling along the same excited-state trajectory as shown in panels a and b.

hot electron (Figure 5a) and a hot hole (Figure 5b) for complex **5c**, in which the hot hole shows a fast mono-exponential decay (Figure 5d), while the hot electron shows slow biexponential decays (Figure 5c). Initially, photo-excitation generates the electron−hole pair by promoting an electron from the occupied state, creating a hole (blue areas in panels a and b of Figure 5) to the unoccupied state (yellow areas in panels a and b of Figure 5). The changes in population of each electron/hole state over time are characterized by the intermediate lifetime and a certain pattern of charge density distribution (insets of MOs in panels a and b of Figure 5). For electron dynamics, there is a fast transition from the initial excited state (LUMO+4) delocalized over the metal center and the N_2O_2-*m*ADIPY ligand to the state mainly localized on the metal (Figure 5a). This initial electron relaxation (hot electron cooling) is fast due to strong NA couplings associated with metal-involved vibrational modes. Recent studies of non-radiative relaxation dynamics in $IrBr_6^{2-}$ and $IrCl_6^{2-}$ by means of ultrafast broadband transient absorption spectroscopy have shown a similar fast 100−400 fs transition from the initially excited LMCT state(s) to the metal-center (MC) state, rationalized by the Jahn−Teller effect.[29−31]

Subsequently, there are slow transitions from electronic states contributed from the In(III) metal to the states that originated from the nitrobenzene substitute of the N_2O_2-

https://doi.org/10.1021/acs.jpclett.2c02115
J. Phys. Chem. Lett. 2022, 13, 9210−9220

*m*ADIPY ligand (LUMO and LUMO+1) (Figure 5a). Due to the low degree of spatial overlap between these electronic states and their mismatch with the related vibrational modes, NA couplings are very weak. Therefore, the resultant electron relaxation to LUMO is much slower than the initial relaxation involving metal-localized states, giving the overall slow biexponential decay of excited electrons. This contrasts with the fast single-exponential dynamics of holes (hot-hole cooling), which involves transitions between states originated from only the N_2O_2-*m*ADIPY ligand, providing strong NA couplings associated with dipyrrin-centered vibrational modes (Figure 5b).

Similar characters of electron and hole states are observed in complexes **1**, **3**, and **5**, rationalizing faster hole cooling than electron cooling (Figures S7−S11). We note that the change in the GGA PBE functional to the hybrid PBE0 does not change the hole cooling or biexponential kinetics of electron cooling, except slightly slows the electron relaxation rate (Figure 5c,d). Faster electron relaxation calculated by PBE is rationalized by underestimated splitting between energy levels, compared to those obtained by PBE0, due to the well-known electron self-interaction problem of GGA functionals.[32] However, observed similarities in carrier decay kinetics and insignificant changes in localization and delocalization properties of electronic states point out the negligible effect of the density functional on the qualitative trends of carrier dynamics in considered complexes. This is also confirmed by good qualitative agreement, excluding a consistent red-shift, between absorption spectra calculated by TDDFT using the PBE0 functional and LANL2DZ/6-31G* basis set implemented in Gaussian-16 and single-particle KS-orbital approach using the PBE functional and the plane wave basis set implemented in VASP, as shown in Figure S12.

On the basis of the results presented in Figure 5, we conclude that the metal-associated electronic states play a critical role in slowing carrier relaxation. The electronic states associated with the In(III) metal center are much more sensitive to the structural distortions that originated from thermal fluctuations, because even insignificant changes in the ligand field result in noticeable energy splitting between the electronic levels of the d orbitals of the metal. Therefore, thermal fluctuations of metal-localized electronic states (Figure S8−S11) along the adiabatic trajectory are the strongest, compared to states delocalized over the ligand (shown by the Kohn−Sham energy band fluctuations in Figure S13). This leads to several overlaps (avoided crossing) with the nearest states, despite a significant energy splitting between them. Such overlaps increase the probability of electron transitions between metal-localized states and ligand-delocalized states during NAMD, if related NA couplings are larger than zero. Thus, the larger the number of such overlaps, the faster the intraband relaxation of electrons.

Annulation increases the rigidity of ligands, thus resulting in a slight reduction in the number of fluctuations, which consequently leads to the reduced number of avoided crossings for metal-localized states. Therefore, electron cooling for all saturated complexes **b** is slower than for non-annulated complexes **a** (Figure 4 and Figures S8−11). However, unsaturated annulation of complexes **c** also increases the level of delocalization of low electronic orbitals over that of the conjugated dipyrrin ligand (Figure S2), which increases the number of NA couplings between these states and hybridized states with both metal and ligand contributions. This interplay between a rigidity effect reducing avoided crossing and conjugation increasing NA couplings balances each other and results in comparable electron cooling of complexes **3a** and **3c** (Figure 4a and Figure S10). However, the EW substituent in complexes **5** destroys this balance due to the increased level of localization of electronic orbitals on the substituting group, which reduces the number NA couplings with metal−ligand delocalized states, resulting in quite slow and biexponential electron relaxation of **5c**, compared to those of **5b** and **5a** (Figure 4b and Figure S11).

Overall, for complexes with dominating π,π^* character in their lowest optical transitions, such as complexes **1** and **3**, the saturated annulation (**1b** and **3b**) slows electron cooling due to reduced avoided crossing, when compared to non-annulated (**1a** and **3a**) and unsaturated (**1c** and **3c**) annulation. In contrast, for complexes with dominating ILCT character in their optical transitions (**5a−c** with strong EW substituents), the unsaturated annulation results in the slowest electron cooling of **5c** compared to those of **5b** and **5a** (Figure 4a,b and Figure S7), due to the decreased number of NA couplings that originated from reduced spatial overlap between metal-associated and ligand-localized electronic states that are involved in interband relaxation dynamics.

These results are complemented by our analysis of the low-energy vibrational modes that contribute to the non-adiabatic dynamics of the complexes. We have computed the density of states (DOS) of vibrational normal modes (Figure S14), as described in Methods. As depicted in panels a and b of Figure S8, for series **1** and **3** of primarily $\pi \rightarrow \pi^*$ optical character, both unsaturated and saturated annulation provide a red-shift and broadening of the vibrational DOS compared to the unannulated complexes. Analysis of displacement coordinates shows that the lowest-energy modes are dominated by in-plane motion of the In(III) ion for unannulated complexes, while upon annulation, the In(III) ion motion becomes out-of-plane (Figure S15). For series **5** of primarily ILCT optical character (Figure S14c), we see a similar trend of red-shift and broadening of the vibrational DOS upon annulation. However, analysis of displacement coordinates shows that the NO_2 substituting group provides some additional contribution with the In(III) ion motion for complexes **5** (Figure S15), which reduces the number of NA couplings with electronic states that originated from the metal center and dipyrrin ligands.

Signs of the discussed trend are also reflected in the nonradiative rates contributed by the intraband (HOMO−LUMO) electron−hole recombination, as shown in Figure 6a

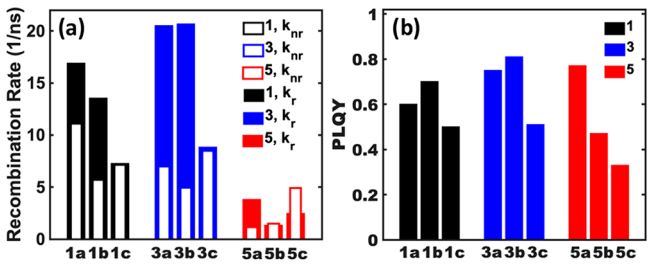

Figure 6. (a) Radiative (filled wide bars) and nonradiative (empty narrow bars) recombination rate constants and (b) photoluminescence quantum yields (PLQYs) for complexes **1** (black), **3** (blue), and **5** (red) with varying ED and EW groups. The empty bars (k_{nr}) are placed atop the filled bars (k_r).

https://doi.org/10.1021/acs.jpclett.2c02115
J. Phys. Chem. Lett. 2022, 13, 9210−9220

(empty bars). For complexes with dominating π,π^* character (complexes **1a**−**c** and **3a**−**c**), saturated annulation minimizes the nonradiative recombination rate due to increased rigidity that reduces the number of both avoided crossing and NA couplings. Unsaturated annulation, however, increases the level of delocalization of both HOMO and LUMO, leading to an increased number of NA couplings involving vibrational modes associated with the dipyrrin ligand, and, thus, increases nonradiative recombination rates of **1c** an **3c**, compared to those of **1b** and **3b**. In contrast, complexes **5a**−**c**, with a strong EW substituent leading to a dominating ILCT character of their lowest optical transitions, demonstrate significantly reduced nonradiative recombination rates, compared to those of corresponding complexes **1a**−**c** and **3a**−**c**, independent of the rigidity of the complexes. In the case of complexes **5a**−**c**, the number of NA couplings is reduced due to a mismatch between spatial localization of the hole (HOMO) and electron (LUMO) states, with holes involving vibrational modes associated with dipyrrin, while electrons mainly involving vibrations originated from the *meso*-phenyl group (insets of panels a and b of Figure 5).

Radiative recombination rates (Figure 6a, filled bars), associated with the intensity of the S_1 transition in the integrated PL spectra (Figure 4c,d), significantly decrease for both saturated and unsaturated annulation in complexes **5b** and **5c**, which can be rationalized by the increased ILCT character of the S_1 transition in complexes **5b** and **5c** compared to that in **5a**. However, for complexes **3a**−**c** with majority π,π^* character, only unsaturated annulation results in decreased emission intensity (Figure 4c) and related radiative rate (Figure 6a). This is in qualitative agreement with our TDDFT calculations (Figure 1 and Figures S1 and S2). As a result, the PLQY (Figure 6b and Table S7) that is computed on the basis of the radiative and nonradiative rate constants according to eqs 12 and 13 is maximal for the saturated annulated complexes with dominating π,π^* character (**1b** and **3b**), which correlates with having the smallest nonradiative recombination rates. However, for complexes with dominating ILCT character of S_1, we observe that complexes with both saturated (**5b**) and unsaturated (**5c**) annulation have reduced PLQYs that correlate with reduced radiative rates. It is worth noting that the calculated PLQY of complex **3a** (60%) is comparable to the experimental value (67%) for the In(III) complex with the *meso*-mesityl N_2O_4DIPY ligand[11] (a complex analogous to **3a**), which validates our computational results.

In summary, we have computationally investigated the effects of EW and ED substituents at the *meso*-phenyl group of the N_2O_2-*m*ADIPY ligand and the ligand structural rigidity associated with annulation on the optical spectra and PLQY of a series of N_2O_2-*m*ADIPY In(III) complexes. Our calculations confirm the hypothesis that annulation of the pyrrole and phenyl groups on the N_2O_2-*m*ADIPY ligand via saturated or unsaturated bridging improves the PLQY of the In(III) complexes by increasing the structural rigidity and, consequently, suppresses the vibrational modes contributing to nonradiative recombination. However, this effect benefits only complexes with primarily π,π^* character for their lowest optical transitions. Both EW substituents and annulation lead to noticeable red-shifts of both the lowest-energy absorption (from 2.2 to 1.8 eV) and emission (from 2.0 to 1.5 eV) to the NIR region. Independent of annulation, the EW substituents result in increased ILCT character in the lowest optical transitions due to stronger localization of the electron density on the *meso*-phenyl groups, compared to the dominating π,π^* character in complexes lacking the EW substituents.

Our NAMD calculations demonstrate a significant difference in electron/hole cooling behaviors, nonradiative electron−hole recombination, and PLQYs between complexes with primarily π,π^* character and those with ILCT character. For complexes with dominant π,π^* character, saturated annulation slows hot-electron and hot-hole cooling and reduces the rate of nonradiative electron−hole recombination, which increases the PLQY and reaches a maximum computed PLQY of 81% for complex **3b**. These trends are rationalized by a rigidity effect induced by saturated annulation that reduces both avoided crossing and NA coupling. However, unsaturated annulation in complexes with π,π^* character results in a balance between molecular rigidity and conjugation, with the latter increasing the number of NA couplings and leading to increased nonradiative rates and reduced PLQYs.

For complexes with dominant ILCT character (**5a**−**c** with strong EW substituents), both saturated and unsaturated annulation cause the slowest biexponential carrier cooling kinetics and reduce the radiative and nonradiative recombination rates. This behavior is attributed to a mismatch between spatial localization of the hole and electron states, which reduces the related transition oscillator strength contributing to the radiative recombination and the NA couplings contributing to the nonradiative recombination. As a result of the interplay between radiative and nonradiative processes, the increased structural rigidity in annulated complexes with significant ILCT character gives rise to the lowest PLQY. Overall, our study shows that In(III) complexes without a substituent or with ED substituents at the *meso*-phenyl group of the N_2O_2-*m*ADIPY ligands and those non-annulated or annulated with saturated bridging show promise as efficient NIR emitting materials due to suppression of vibrational modes contributing to nonradiative recombination.

METHODS

Computational Details. For calculations of the geometries and optical spectra of the studied complexes, we used the Gausian-16 software package.[33] The geometries of all complexes were optimized at the DFT level using the PBE0 functional[34] and the mixed basis sets with LANL2DZ[35] assigned to In(III) and 6-31G* to all other atoms.[36,37] Calculations were performed in an acetonitrile solvent incorporated via a conductor polarized continuum model (CPCM).[38,39] Optical transitions were calculated by applying linear response TDDFT[40] using the same functional, basis set, and solvent model that were used for the geometry optimization. For absorption spectra, 30 singlet optical transitions were computed and broadened by the empirical Gaussian function using a line width of 0.1 eV to reproduce the thermal broadening of the typical experimental spectra. This approach has previously provided reasonable agreement with experimental absorption spectra for many Ir(III) complexes,[41] and the result qualitatively agrees with the experimental data of **3a**.[12,11]

To simulate fluorescence spectra, we used analytical gradient TDDFT (AG-TDDFT),[13,14] which provides optimization of excited state S_1. To include vibronic features in the profile of absorption and fluorescence spectra, Franck−Condon (FC) progression[42,43] for the first optical transition was computed for each complex, using the same methodology that was used for TDDFT calculations. The optical transitions were

https://doi.org/10.1021/acs.jpclett.2c02115
J. Phys. Chem. Lett. 2022, 13, 9210−9220

characterized by natural transition orbitals (NTOs)[44] and visualized in VMD[45] with a isovalue of 0.02.

For photoexcited non-adiabatic molecular dynamics (NAMD), we used VASP.[46] The electronic structure of our atomistic models was found using DFT with the Perdew–Burke–Ernzerhof (PBE) functional[34] and PBE0 hybrid functional in a plane wave basis set along with projector augmented wave (PAW) pseudopotential,[47,48] as implemented in VASP.[46] Vacuum layers were introduced to spatially separate the replica models across the periodic boundaries, resulting in computational cell dimensions for each model of 19.5 Å × 19.5 Å × 19.5 Å. To initialize adiabatic molecular dynamics (AMD), the model was set to a Nose-Hoover thermostat[49] and heated to 300 K. Once the temperature was reached, the AMD trajectory was propagated for 1 ps using a time step of 1 fs under the *NVT* microcanonical ensemble where free energy remains constant.

Methodology of NAMD and PLQY Calculations. To dynamically couple electronic and nuclear degrees of freedom, we first used adiabatic molecular dynamics (AMD). This provides kinetic energy of nuclei to break the orthogonality of the electronic states. The nuclear degrees of freedom are treated in the classical path approximation (CPA)[50] with the nuclei following the classical path trajectories. The initial velocities of nuclei are scaled to keep a constant temperature (eq 1), with forces acting on the nuclei depending on the electronic density (eq 2)

$$\sum_{I=1}^{N^{\text{ion}}} \frac{M_I}{2}\left(\frac{\mathrm{d}\vec{R}_I}{\mathrm{d}t}\bigg|_{t=0}\right)^2 = \frac{3}{2}N^{\text{ion}}k_{\text{B}}T \tag{1}$$

$$\frac{\mathrm{d}^2}{\mathrm{d}t^2}\vec{R}_I = \vec{F}_I[\hat{\rho}]/M_I \tag{2}$$

where $\vec{R}_I$ represents ionic coordinates, M_I is the mass of the Ith nuclei, k_{B} is the Boltzmann constant, T is the temperature, and $\vec{F}_I[\hat{\rho}]$ is the force acting on the ions as a functional of DFT-computed electron density $\hat{\rho}$.

The time evolution of electronic degrees of freedom that are weakly coupled to a thermal bath can be described using the Redfield quantum master equation[24,25] in the density matrix formalism.

$$\frac{\mathrm{d}}{\mathrm{d}t}\rho_{ij} = -\frac{i}{\hbar}\sum_k (F_{ik}\rho_{kj} - \rho_{ik}F_{kj}) + \left(\frac{\mathrm{d}\rho_{ij}}{\mathrm{d}t}\right)_{\text{diss}} \tag{3}$$

where F is the many-electron Fock matrix, which includes exchange and correlation, and ρ is the density matrix. Note that the Fock matrix consists of only diagonal elements represented by Kohn–Sham (KS) energies. Thus, the first term in eq 3 is the Liouville–von Neumann equation describing the unitary time evolution of a closed system, while the second term describes electronic energy dissipation due to weak coupling to a thermal bath. The dissipative transitions result from the quantum part of the nuclear kinetic energy and can be parametrized from NACs, $V_{ij}^{\text{NAC}}(t)$, computed "on the fly"[51] using the adiabatic basis of KS orbitals $\varphi_i(t)$, obtained from DFT-based adiabatic molecular dynamics:[52]

$$V_{ij}^{\text{NAC}}(t) = -i\hbar\left\langle \varphi_i(t)\middle|\frac{\partial}{\partial t}\middle|\varphi_j(t)\right\rangle \tag{4}$$

Due to the nuclear kinetic energy, the orthogonality relation is broken and provides a "mixing" of KS orbitals.

NACs are converted into rates of transitions by taking the Fourier transform of the autocorrelation function, $M_{ijkl}(\tau)$, which provides components for the Redfield tensor, R_{ijkl}:

$$M_{ijkl}(\tau) = \frac{1}{T}\int_0^T V_{ij}^{\text{NAC}}(t+\tau)V_{kl}^{\text{NAC}}(t)\,\mathrm{d}t \tag{5a}$$

$$\Gamma_{ijkl}^{+} = \frac{1}{T}\int_0^T M_{ijkl}(\tau)\mathrm{e}^{-i\omega_{kl}\tau}\,\mathrm{d}\tau \tag{5b}$$

$$\Gamma_{ijkl}^{-} = \frac{1}{T}\int_0^T M_{ijkl}(\tau)\mathrm{e}^{-i\omega_{ij}\tau}\,\mathrm{d}\tau \tag{5c}$$

$$R_{ijkl} = \Gamma_{ijkl}^{+} + \Gamma_{ijkl}^{-} + \delta_{lj}\sum_m \Gamma_{ijkl}^{+} - \delta_{ik}\sum_m \Gamma_{ijkl}^{-} \tag{5d}$$

The Redfield tensor, eq 5d, controls the dissipative term in eq 3:

$$\left(\frac{\mathrm{d}\rho_{ij}}{\mathrm{d}t}\right)_{\text{diss}} = \sum_{lm} R_{ijlm}\rho_{lm} \tag{6}$$

Here we employ an independent particle approximation[53] assuming that the dynamics of the electron occupations in conduction band ρ_{ii} ($i \le$ HOMO) and hole occupations in valence band ρ_{jj} ($j \ge$ LUMO) occur independently.[54] Nonradiative recombination of charge carriers is accounted for by transforming the off-diagonal Redfield tensor $R_{ii,jj}$ elements into single-exponential dampening of the excited state[55]

$$\frac{\partial}{\partial t}\begin{pmatrix}\tilde{\rho}_{ii}\\ \tilde{\rho}_{jj}\end{pmatrix} = \sum_{i',j'}\begin{pmatrix}R_{ii,i'i'} & 0\\ 0 & R_{jj,j'j'}\end{pmatrix}\begin{pmatrix}\tilde{\rho}_{i'i'}\\ \tilde{\rho}_{j'j'}\end{pmatrix} \tag{7}$$

with the ansatz $\tilde{\rho}_{ii} = \rho_{ii}\mathrm{e}^{-R_{ii,ii}t}$ and $\tilde{\rho}_{jj} = \rho_{jj}\mathrm{e}^{-R_{jj,jj}t}$.[53]

Observables along the excited-state trajectory are found from expected values computed in terms of the density matrix. The population density in the energy domain is described as

$$n(\varepsilon, t) = \sum_i \tilde{\rho}_{ii}(t)\delta(\varepsilon - \varepsilon_i) \tag{8a}$$

where ε_i terms are eigen energies of the KSO equation. In the excited state, the non-equilibrium density is

$$\Delta n(\varepsilon, t) = n(\varepsilon, t) - n^{\text{eq}}(\varepsilon, t) \tag{8b}$$

where $n^{\text{eq}}(\varepsilon, t)$ is the ground-state equilibrium density, $\Delta n(\varepsilon, t) > 0$ represents an increase in electron density, $\Delta n(\varepsilon, t) < 0$ indicates an increase in hole density, and $\Delta n(\varepsilon, t) = 0$ represents an unchanged population. The electron (eq 9a) and hole (eq 9b) energy expectation value along the trajectory is described as

$$\langle \Delta\varepsilon_{\text{e}}\rangle(t) = \sum_{i\ge\text{LU}} \tilde{\rho}_{ii}(t)\varepsilon_i(t) \tag{9a}$$

$$\langle \Delta\varepsilon_{h}\rangle(t) = \sum_{i\le\text{HO}} \tilde{\rho}_{ii}(t)\varepsilon_i(t) \tag{9b}$$

where the electron state is summed over the occupations in the conduction band and the hole state is summed over the valence band. The charge carrier energy expectation value is normalized to a dimensionless energy

https://doi.org/10.1021/acs.jpclett.2c02115
J. Phys. Chem. Lett. 2022, 13, 9210−9220

$$\langle E_{e/h}\rangle(t) = \frac{\langle \Delta\varepsilon_{e/h}\rangle(t) - \langle \Delta\varepsilon_{e/h}\rangle(\infty)}{\langle \Delta\varepsilon_{e/h}\rangle(0) - \langle \Delta\varepsilon_{e/h}\rangle(\infty)} \tag{10a}$$

Assuming a single-exponential decay, the rate of relaxation for a "hot" electron to the conduction band edge LUMO state is

$$k_{e/h} = (\tau^{e/h})^{-1} = \left[\int_0^\infty \langle E_{e/h}\rangle(t)\, dt\right]^{-1} \tag{10b}$$

Equations 10a and 10b describe the nonradiative energy decay and kinetics of charge carriers along the excited-state trajectory by emitting a phonon. A competing relaxation pathway for charge carriers is emission of a photon. The time-resolved emission along the excited-state trajectory is described as

$$E(\hbar\omega, t) = \sum_{j>i} f_{ij}\delta(\hbar\omega - \hbar\omega_{ij})[\tilde{\rho}_{jj}(t) - \tilde{\rho}_{ii}(t)] \tag{11a}$$

where f_{ij} is the oscillator strength between states i and j, $\delta(\hbar\omega - \hbar\omega_{ij})$ gives the energy of the transition, and the $\tilde{\rho}_{ii}(t) - \tilde{\rho}_{ii}(t)$ terms describes the population inversion needed for photoluminescence to occur. To generate a PL spectrum, the time-resolved emission (eq 10a) is summed over the length of the trajectory

$$E^{tot}(\hbar\omega) = \frac{1}{T}\int_0^T E(\hbar\omega, t)\, dt \tag{11b}$$

where T is the duration of the trajectory.

To compute a PLQY from the excited-state dynamics, we approximate the nonradiative and radiative relaxation rates as the matrix elements of the Redfield tensor (eq 12a) and the Einstein coefficient for spontaneous recombination (eq 12b) that corresponds to the lowest-energy transitions across the bandgap

$$k_{nr} \approx R_{HOMO-LUMO} \tag{12a}$$

$$k_r \approx A_{HOMO-LUMO} = \frac{8\pi^2 \nu_{HO-LU}{}^2 e^2}{\varepsilon_0 m_e c^3} f_{HO-LU} \tag{12b}$$

where ν_{HO-LU} is the transition energy and f_{HO-LU} the oscillator strength associated with the HOMO−LUMO optical transition, All other terms represent the usual fundamental constants.

PLQY is defined as the ratio of the radiative recombination rate to the sum of radiative and nonradiative recombination (eq 12).

$$PLQY = \frac{k_r}{k_r + k_{nr}} \tag{13}$$

Calculations of Vibrational Modes. To analyze the impact of annulation on the vibrational modes of the complexes, we compute normal modes by diagonalizing the dynamical matrix giving normal mode eigenvectors ζ_n with eigenvalues ν_n, as implemented in VASP 5.4 using the finite-elements approach. The distribution of vibrational modes is described as

$$g(\nu_n) = \frac{1}{N}\sum_n \delta(\hbar\nu - \hbar\nu_n)$$

where ν_n is the mode frequency in inverse centimeters, N is the number of normal modes, and the δ function is broadened using a Gaussian function.

■ ASSOCIATED CONTENT

Supporting Information

The Supporting Information is available free of charge at https://pubs.acs.org/doi/10.1021/acs.jpclett.2c02115.

TDDFT and AG-TDDFT spectra, NTOs for state S_1, ground-state and excited-state structural analysis, Franck−Condon contributions to TDDFT spectra, KSO fluctuations along the AMD trajectory, comparison of hot carrier cooling kinetics and luminescence, radiative and nonradiative trajectories for each complex, and a comparison of TDKS and TDDFT spectra (PDF)

■ AUTHOR INFORMATION

Corresponding Author

Svetlana Kilina − *Department of Chemistry and Biochemistry, North Dakota State University, Fargo, North Dakota 58108, United States;* orcid.org/0000-0003-1350-2790; Email: svetlana.kilina@ndsu.edu

Authors

Aaron Forde − *Department of Chemistry and Biochemistry and Materials and Nanotechnology Program, North Dakota State University, Fargo, North Dakota 58108, United States; Theoretical Division and Center for Nonlinear Studies, Los Alamos National Laboratory, Los Alamos, New Mexico 87545, United States;* orcid.org/0000-0001-6245-8584

Levi Lystrom − *Shock and Detonation Physics, Los Alamos National Laboratory, Los Alamos, New Mexico 87545, United States;* orcid.org/0000-0001-6369-8643

Wenfang Sun − *Department of Chemistry and Biochemistry, North Dakota State University, Fargo, North Dakota 58108, United States;* orcid.org/0000-0003-3608-611X

Dmitri Kilin − *Department of Chemistry and Biochemistry, North Dakota State University, Fargo, North Dakota 58108, United States;* orcid.org/0000-0001-7847-5549

Complete contact information is available at: https://pubs.acs.org/10.1021/acs.jpclett.2c02115

Notes

The authors declare no competing financial interest.

■ ACKNOWLEDGMENTS

Calculations of NIR absorption and emission of the In(III) complexes were supported by the National Science Foundation (NSF) under Grant CHE-1800476. S.K. and D.K. acknowledge the support of the U.S. Department of Energy (DOE) under Grant DE-SC0022239 for study of Near-Infrared Emissive Metal-Organic Complexes and PLQY calculations in molecular systems. A.F. acknowledges NSF-1944921 for method development of the non-adiabatic dynamics. This work used resources of the Center for Computationally Assisted Science and Technology (CCAST) at North Dakota State University, which were made possible in part by NSF MRI Award 2019077. For additional computational resources used for simulations of non-adiabatic dynamics, the authors acknowledge the National Energy Research Scientific Computing Center (NERSC), supported by the Office of Science of the DOE. This work was also performed in part at the Center for Nonlinear Studies (CNLS) and the Center for Integrated Nanotechnology (CINT), a DOE Office of Basic Energy Sciences user facility at the Los Alamos National Laboratory (LANL). A.F. and D.K. thank Yulun Han, Amir Alesadi, Sarah

Ghazanfari, David Graupner, Meade Erickson, Kamrun Nahar Keya, and Landon Johnson for editorial comments during development of the manuscript.

REFERENCES

(1) Zhao, J.; Wu, W.; Sun, J.; Guo, S. Triplet photosensitizers: from molecular design to applications. *Chem. Soc. Rev.* **2013**, *42* (12), 5323−5351.
(2) Li, K.; Chen, Y.; Wang, J.; Yang, C. Diverse emission properties of transition metal complexes beyond exclusive single phosphorescence and their wide applications. *Coord. Chem. Rev.* **2021**, *433*, 213755.
(3) Kubo, Y.; Minowa, Y.; Shoda, T.; Takeshita, K. Synthesis of a new type of dibenzopyrromethene−boron complex with near-infrared absorption property. *Tetrahedron Lett.* **2010**, *51* (12), 1600−1602. Lakshmi, V.; Rajeswara Rao, M.; Ravikanth, M. Halogenated boron-dipyrromethenes: synthesis, properties and applications. *Organic & Biomolecular Chemistry* **2015**, *13* (9), 2501−2517.
(4) Yamamura, M.; Albrecht, M.; Albrecht, M.; Nishimura, Y.; Arai, T.; Nabeshima, T. Red/Near-Infrared Luminescence Tuning of Group-14 Element Complexes of Dipyrrins Based on a Central Atom. *Inorg. Chem.* **2014**, *53* (3), 1355−1360.
(5) Makarova, E. A.; Zatsikha, Y. V.; Newman, K. M. E.; Paidi, V. K.; Beletsky, V. A.; van Lierop, J.; Lukyanets, E. A.; Nemykin, V. N. Direct Synthesis of an Unprecedented Stable Radical of Nickel(II) 3,5-Bis(dimedonyl)azadiisoindomethene with Strong and Narrow Near-Infrared Absorption at $\lambda \sim 1000$ nm. *Inorg. Chem.* **2017**, *56* (11), 6052−6055.
(6) Zhou, X.; Yu, C.; Feng, Z.; Yu, Y.; Wang, J.; Hao, E.; Wei, Y.; Mu, X.; Jiao, L. Highly Regioselective α-Chlorination of the BODIPY Chromophore with Copper(II) Chloride. *Org. Lett.* **2015**, *17* (18), 4632−4635.
(7) Song, H.; Rajendiran, S.; Koo, E.; Min, B. K.; Jeong, S. K.; Daniel Thangadurai, T.; Yoon, S. Fluorescence enhancement of N2O2-type dipyrrin ligand in two step responding to zinc(II) ion. *J. Lumin.* **2012**, *132* (11), 3089−3092.
(8) Jortner, J. Radiationless transitions. *Pure Appl. Chem.* **1971**, *27* (3), 389−420.
(9) Lin, S. H. Energy Gap Law and Franck−Condon Factor in Radiationless Transitions. *J. Chem. Phys.* **1970**, *53* (9), 3766−3767.
(10) Luo, X.; Li, J.; Zhao, J.; Gu, L.; Qian, X.; Yang, Y. A general approach to the design of high-performance near-infrared (NIR) D-π-A type fluorescent dyes. *Chin. Chem. Lett.* **2019**, *30* (4), 839−846.
(11) Sumiyoshi, A.; Chiba, Y.; Matsuoka, R.; Noda, T.; Nabeshima, T. Efficient luminescent properties and cation recognition ability of heavy group 13 element complexes of N2O2- and N2O4-type dipyrrins. *Dalton Transactions* **2019**, *48* (35), 13169−13175.
(12) Lystrom, L.; Shukla, M.; Sun, W.; Kilina, S. Extending Fluorescence of meso-Aryldipyrrin Indium(III) Complexes to Near-Infrared Regions via Electron Withdrawing or π-Expansive Aryl Substituents. *J. Phys. Chem. Lett.* **2021**, *12* (33), 8009−8015.
(13) Furche, F.; Ahlrichs, R. Adiabatic time-dependent density functional methods for excited state properties. *J. Chem. Phys.* **2002**, *117* (16), 7433−7447.
(14) Van Caillie, C.; Amos, R. D. Geometric derivatives of density functional theory excitation energies using gradient-corrected functionals. *Chem. Phys. Lett.* **2000**, *317* (1), 159−164.
(15) Liu, B.; Jabed, M. A.; Guo, J.; Xu, W.; Brown, S. L.; Ugrinov, A.; Hobbie, E. K.; Kilina, S.; Qin, A.; Sun, W. Neutral Cyclometalated Iridium(III) Complexes Bearing Substituted N-Heterocyclic Carbene (NHC) Ligands for High-Performance Yellow OLED Application. *Inorg. Chem.* **2019**, *58* (21), 14377−14388. Wang, L.; Monro, S.; Cui, P.; Yin, H.; Liu, B.; Cameron, C. G.; Xu, W.; Hetu, M.; Fuller, A.; Kilina, S.; et al. Heteroleptic Ir(III)N6 Complexes with Long-Lived Triplet Excited States and in Vitro Photobiological Activities. *ACS Appl. Mater. Interfaces* **2019**, *11* (4), 3629−3644.
(16) Wang, L.; Cui, P.; Liu, B.; Kilina, S.; Sun, W. Novel N6 trisbidentate ligand coordinated Ir(iii) complexes and their Ru(ii) analogs. *Dalton Transactions* **2018**, *47* (39), 13776−13780.
(17) Liu, B.; Gao, Y.; Jabed, M. A.; Kilina, S.; Liu, G.; Sun, W. Lysosome Targeting Bis-terpyridine Ruthenium(II) Complexes: Photophysical Properties and In Vitro Photodynamic Therapy. *ACS Applied Bio Materials* **2020**, *3* (9), 6025−6038.
(18) Lu, T.; Wang, C.; Lystrom, L.; Pei, C.; Kilina, S.; Sun, W. Effects of extending the π-conjugation of the acetylide ligand on the photophysics and reverse saturable absorption of Pt(ii) bipyridine bisacetylide complexes. *Phys. Chem. Chem. Phys.* **2016**, *18* (41), 28674−28687.
(19) Vittardi, S. B.; Magar, R. T.; Schrage, B. R.; Ziegler, C. J.; Jakubikova, E.; Rack, J. J. Evidence for a lowest energy 3MLCT excited state in [Fe(tpy)(CN)3]−. *Chem. Commun.* **2021**, *57* (38), 4658−4661.
(20) Myers, T. W.; Bjorgaard, J. A.; Brown, K. E.; Chavez, D. E.; Hanson, S. K.; Scharff, R. J.; Tretiak, S.; Veauthier, J. M. Energetic Chromophores: Low-Energy Laser Initiation in Explosive Fe(II) Tetrazine Complexes. *J. Am. Chem. Soc.* **2016**, *138* (13), 4685−4692.
(21) High, J. S.; Rego, L. G. C.; Jakubikova, E. Quantum Dynamics Simulations of Excited State Energy Transfer in a Zinc−Free-Base Porphyrin Dyad. *J. Phys. Chem. A* **2016**, *120* (41), 8075−8084.
(22) Nelson, T.; Fernandez-Alberti, S.; Roitberg, A. E.; Tretiak, S. Electronic Delocalization, Vibrational Dynamics, and Energy Transfer in Organic Chromophores. *J. Phys. Chem. Lett.* **2017**, *8* (13), 3020−3031.
(23) Fernandez-Alberti, S.; Roitberg, A. E.; Kleiman, V. D.; Nelson, T.; Tretiak, S. Shishiodoshi unidirectional energy transfer mechanism in phenylene ethynylene dendrimers. *J. Chem. Phys.* **2012**, *137* (22), 22A526.
(24) Redfield, A. G. On the Theory of Relaxation Processes. *IBM J. Res. Dev.* **1957**, *1* (1), 19−31.
(25) Jean, J. M.; Friesner, R. A.; Fleming, G. R. Application of a multilevel Redfield theory to electron transfer in condensed phases. *J. Chem. Phys.* **1992**, *96* (8), 5827−5842.
(26) Forde, A.; Inerbaev, T.; Hobbie, E. K.; Kilin, D. S. Excited-State Dynamics of a CsPbBr3 Nanocrystal Terminated with Binary Ligands: Sparse Density of States with Giant Spin−Orbit Coupling Suppresses Carrier Cooling. *J. Am. Chem. Soc.* **2019**, *141* (10), 4388−4397.
(27) Forde, A.; Inerbaev, T.; Kilin, D. Spectral Signatures of Positive and Negative Polarons in Lead-Halide Perovskite Nanocrystals. *J. Phys. Chem. C* **2020**, *124* (1), 1027−1041.
(28) Hilborn, R. C. Einstein coefficients, cross sections, f values, dipole moments, and all that. *American Journal of Physics* **1982**, *50* (11), 982−986.
(29) Budkina, D. S.; Gemeda, F. T.; Matveev, S. M.; Tarnovsky, A. N. Ultrafast Dynamics in LMCT And Intraconfigurational Excited States in Hexahaloiridates(IV), Models For Heavy Transition Metal Complexes and Building Blocks of Quantum Correlated Materials. *Phys. Chem. Chem. Phys.* **2020**, *22* (30), 17351−17364.
(30) Matveev, S. M.; Budkina, D. S.; Zheldakov, I. L.; Phelan, M. R.; Hicks, C. M.; Tarnovsky, A. N. Femtosecond Dynamics of Metal-centered and Ligand-to-metal Charge-transfer (t(2g)-based) Electronic Excited States in Various Solvents: A Comprehensive Study of IrBr62. *J. Chem. Phys.* **2019**, *150* (5), 054302.
(31) Li, C.; Kong, X. Y.; Tan, Z. H.; Yang, C. T.; Soo, H. S. Emergence of Ligand-to-metal Charge Transfer in Homogeneous Photocatalysis and Photosensitization. *Chemical Physics Reviews* **2022**, *3* (2), 021303.
(32) Kilina, S.; Kilin, D.; Tretiak, S. Light-Driven and Phonon-Assisted Dynamics in Organic and Semiconductor Nanostructures. *Chem. Rev.* **2015**, *115* (12), 5929−5978.
(33) *Gaussian 16*, rev. C.01; Gaussian, Inc.: Wallingford, CT, 2016.
(34) Perdew, J. P.; Burke, K.; Ernzerhof, M. Generalized Gradient Approximation Made Simple. *Phys. Rev. Lett.* **1996**, *77* (18), 3865−3868.

https://doi.org/10.1021/acs.jpclett.2c02115
J. Phys. Chem. Lett. 2022, 13, 9210−9220

(35) Wadt, W. R.; Hay, P. J. Ab initio effective core potentials for molecular calculations. Potentials for main group elements Na to Bi. *J. Chem. Phys.* **1985**, *82* (1), 284−298.
(36) Francl, M. M.; Pietro, W. J.; Hehre, W. J.; Binkley, J. S.; Gordon, M. S.; DeFrees, D. J.; Pople, J. A. Self-consistent molecular orbital methods. XXIII. A polarization-type basis set for second-row elements. *J. Chem. Phys.* **1982**, *77* (7), 3654−3665.
(37) Krishnan, R.; Binkley, J. S.; Seeger, R.; Pople, J. A. Self-consistent molecular orbital methods. XX. A basis set for correlated wave functions. *J. Chem. Phys.* **1980**, *72* (1), 650−654.
(38) Barone, V.; Cossi, M.; Tomasi, J. Geometry optimization of molecular structures in solution by the polarizable continuum model. *J. Comput. Chem.* **1998**, *19* (4), 404−417.
(39) Cossi, M.; Barone, V.; Cammi, R.; Tomasi, J. Ab initio study of solvated molecules: a new implementation of the polarizable continuum model. *Chem. Phys. Lett.* **1996**, *255* (4), 327−335.
(40) Stratmann, R. E.; Scuseria, G. E.; Frisch, M. J. An efficient implementation of time-dependent density-functional theory for the calculation of excitation energies of large molecules. *J. Chem. Phys.* **1998**, *109* (19), 8218−8224.
(41) Wang, C.; Lystrom, L.; Yin, H.; Hetu, M.; Kilina, S.; McFarland, S. A.; Sun, W. Increasing the triplet lifetime and extending the ground-state absorption of biscyclometalated Ir(iii) complexes for reverse saturable absorption and photodynamic therapy applications. *Dalton Transactions* **2016**, *45* (41), 16366−16378. Liu, B.; Lystrom, L.; Kilina, S.; Sun, W. Effects of Varying the Benzannulation Site and π Conjugation of the Cyclometalating Ligand on the Photophysics and Reverse Saturable Absorption of Monocationic Iridium(III) Complexes. *Inorg. Chem.* **2019**, *58* (1), 476−488.
(42) Santoro, F.; Improta, R.; Lami, A.; Bloino, J.; Barone, V. Effective method to compute Franck-Condon integrals for optical spectra of large molecules in solution. *J. Chem. Phys.* **2007**, *126* (8), 084509.
(43) Barone, V.; Bloino, J.; Biczysko, M.; Santoro, F. Fully Integrated Approach to Compute Vibrationally Resolved Optical Spectra: From Small Molecules to Macrosystems. *J. Chem. Theory Comput.* **2009**, *5* (3), 540−554.
(44) Martin, R. L. Natural transition orbitals. *J. Chem. Phys.* **2003**, *118* (11), 4775−4777.
(45) Humphrey, W.; Dalke, A.; Schulten, K. VMD: Visual molecular dynamics. *J. Mol. Graphics* **1996**, *14* (1), 33−38.
(46) Kresse, G.; Furthmüller, J. Efficiency of ab-initio total energy calculations for metals and semiconductors using a plane-wave basis set. *Comput. Mater. Sci.* **1996**, *6* (1), 15−50.
(47) Blöchl, P. E. Projector augmented-wave method. *Phys. Rev. B* **1994**, *50* (24), 17953−17979.
(48) Kresse, G.; Joubert, D. From ultrasoft pseudopotentials to the projector augmented-wave method. *Phys. Rev. B* **1999**, *59* (3), 1758−1775.
(49) Hoover, W. G. Canonical dynamics: Equilibrium phase-space distributions. *Phys. Rev. A* **1985**, *31* (3), 1695−1697.
(50) Mott, N. F. On the Theory of Excitation by Collision with Heavy Particles. *Math. Proc. Cambridge Philos. Soc.* **1931**, *27* (4), 553−560.
(51) Hammes-Schiffer, S.; Tully, J. C. Proton transfer in solution: Molecular dynamics with quantum transitions. *J. Chem. Phys.* **1994**, *101* (6), 4657−4667.
(52) Kresse, G.; Hafner, J. Ab initio molecular dynamics for liquid metals. *Phys. Rev. B* **1993**, *47* (1), 558−561.
(53) Han, Y.; Meng, Q.; Rasulev, B.; May, P. S.; Berry, M. T.; Kilin, D. S. Photoinduced Charge Transfer versus Fragmentation Pathways in Lanthanum Cyclopentadienyl Complexes. *J. Chem. Theory Comput.* **2017**, *13* (9), 4281−4296.
(54) Huang, S. P.; Kilin, D. S. Charge Transfer, Luminescence, and Phonon Bottleneck in TiO_2 Nanowires Computed by Eigenvectors of Liouville Superoperator. *J. Chem. Theory Comput.* **2014**, *10* (9), 3996−4005.
(55) Forde, A.; Kilin, D. Defect Tolerance Mechanism Revealed! Influence of Polaron Occupied Surface Trap States on CsPbBr3 Nanocrystal Photoluminescence: Ab Initio Excited-State Dynamics. *J. Chem. Theory Comput.* **2021**, *17* (11), 7224−7236.

https://doi.org/10.1021/acs.jpclett.2c02115
J. Phys. Chem. Lett. 2022, 13, 9210−9220